Ductilization of aluminium alloy 6056 by friction stir processing

F. Hannard, S. Castin, E. Maire, R. Mokso, T. Pardoen, A. Simar

Ductilization of aluminium alloy 6056 by friction stir processing

F. Hannard[1], S. Castin[1], E. Maire[2], R. Mokso[3,4], T. Pardoen[1], A.Simar[1]

[1] *Institute of Mechanics, Materials and Civil Engineering, Université catholique de Louvain, Place Sainte Barbe 2, B-1348 Louvain-la-Neuve, Belgium*

[2] MATEIS UMR5510, INSA-Lyon, F-69621 Villeurbanne, France

[3] Swiss Light Source, Paul Scherrer Institute, Villigen, 5232, Switzerland

[4]MAX-lab, P.O. Box 118, S-221 00 Lund, Sweden

Corresponding author: Florent Hannard, florent.hannard@uclouvain.be, +32 10 47 24 39

Abstract

The ductility of Al alloys is dictated by the nucleation, growth and coalescence of small internal voids originating from intermetallic particle fracture and from the presence of pre-existing porosity. The ductility is degraded when intermetallic particles are large and clustered. A low ductility adversely impacts both forming operations and the integrity of structural components. Local stirring using a friction stir processing (FSP) tool is shown here to very significantly increase the fracture strain of the Al alloy 6056 sometimes by more than a factor of two while making it more isotropic. Three reasons for the ductilization are unravelled based on 3D microtomography: (i) FSP breaks the large intermetallic particles into smaller, and thus stronger, fragments, (ii) FSP closes the pre-existing porosity; (iii) FSP randomizes the particle distribution. Hence, FSP positively impacts three of the main causes of ductility loss in metallic alloys. From an applicability viewpoint, this method has the potential to locally improve ductility of sheets at locations where forming involves large strains or of structural components at stress concentration points.

Keywords: Friction stir processing, Ductile damage, Tomography, Aluminium Alloys.

1. Introduction

Ductile fracture is characterized by the nucleation of microvoids, followed by stable growth until coalescence of neighboring voids [**1-6**]. The accumulation of void linkage leads to the formation of a macroscopic crack that finally propagates until final failure. Micron-sized iron-rich intermetallic particles constitute the main source of damage in Al alloys. These particles fracture or undergo interface decohesion [**4-8**]. Additionally, voids may be already present from processing or from hydrogen or can also nucleate, usually at large strains, on smaller size dispersoïds [**4**]. Factors like particle clustering, particle morphology and size have a first order impact on the fracture strain [**6**,**9**]. It remains an important scientific and technological

challenge to improve the ductility of Al alloys especially in high strength condition resulting from peak aging heat treatments.

Friction stir welding (FSW) is a solid-state welding process developed to bypass limitations associated with local melting and solidification involved in most conventional welding processes. It is particularly suitable for high strength Al alloys [**10,11**]. Friction stir processing (FSP) is a process derived from FSW [**12-39**], involving a non-consumable tool with complex features to locally modify the microstructure through solid state mixing. The rotating tool penetrates the material until the shoulder gets into contact with the upper surface and is then displaced along the surface at a controlled velocity and rotation speed (see Fig. **1.a)**. The heat generated by friction and deformation leads to a malleable state that promotes material flow from the front to the back of the tool and around the pin. The strain level during FSP is in the 5 to 10 range and the strain rate level is on the order of 10 to 400 s^{-1} [**19**]. FSP leads to a decrease of the grain size by dynamic recrystallization [**20**]. Kumar *et al.* [**21**] have shown a grain size reduction by a factor close to 40 in an Al-Mg-Sc alloy. These fine grains tend to be unstable during subsequent solution heat treatment, typically above 450°C in Al7010 [**22**]. Abnormal grain growth is likely to occur at high temperature in grains free of dislocations or free of pinning phases [**22,23**]. Grains as large as a few millimeters have been reported in FSPed 7xxx series [**22,23**] and cast Al alloys [**24**].

FSP has already been applied to cast Al alloy for the sake of improving properties. Cast Al alloys present large amount of porosities due to gas involved in the molten state, or due to solidification shrinkage defects. FSP has been shown to decrease the microporosity [**12,25-32**] owing to the large pressure applied by the tool at high temperatures, e.g. 0.1% to 0.02% in A356 [**26**]. Such porosity reduction significantly improves the ductility [**26,31,33**]. The cast microstructure is also homogenized and refined by FSP due to the redistribution, erosion and breakage of large particles [**26,28,34**] improving the strength and ductility [**31,35**], e.g. a total

elongation improvement from 1.1% to 20% in Al-7Si-0.5Mg [31]. The fatigue performances of FSPed cast materials are also impressively improved [12,36-38], e.g. 80% increase of fatigue stress level in a cast A356 alloy [12].

The application of FSP to improve wrought Al alloy has not yet been widely studied. In wrought alloy the amount of initial porosity is much smaller than in cast alloys, but the potential for improvement could come from the impact on the intermetallic particles. Cavaliere [39] has shown a promising increase in fatigue resistance for a 2014 Al alloy. Nevertheless, to the best of the authors knowledge, no detailed analysis is available yet in the literature about the impact of FSP on damage resistance of wrought Al alloys. In a previous study [6], we characterized and modelled the ductile failure process of three 6xxx series Al alloys (6005A, 6061 and 6056). The key element controlling the magnitude of the fracture strain in these alloys was the effect of particle size distribution and spatial distribution on the void nucleation and coalescence process. The presence of pre-existing voids has also been shown to have a first order effect on the fracture strain.

The goal of the present study is to investigate, based on microtomography and detailed image analysis, the potential of friction stir processing (FSP) to improve the ductility of Al 6056 plates through the fracture of the large second phase particles into smaller and more resistant fragments, the closing of the existing initial porosity and the homogenization of the particle spatial distribution.

2. Materials and experimental methods

2.1. Materials and FSP

Cold rolled 6 mm thick plates of Al 6056 were used in T4 initial condition. Up to six overlapping FSP passes (see Fig. **1.(a)),** were performed with a tool rotation rate of 500 rpm and a traverse speed of 200 mm/min along the rolling direction (RD) (except for the case of

six passes performed also in the transverse direction (TD)). The tool was composed of a 20 mm diameter scrolled shoulder prolonged by a 5 mm long cylindrical M6 threaded Triflat pin, see Ref. [34]. After FSP, all samples were kept at room temperature for at least 1 month to allow natural ageing. The as-FSPed samples were then heat treated at 180°C, and some of them at 350°C as well. Heat treatments were systematically followed by water quenching.

2.2. SEM and X-ray microtomography

Cross-sectioning of the weld along a plane perpendicular to the FSP direction was performed for metallographic observations (Fig. **1**). After standard polishing, the intermetallic particles were characterized based on images taken with a Field Emission Gun Scanning Electron Microscope (FEG-SEM) operated at 15 kV under electron backscattered mode and analyzed using the software ImageJ [40]. X-ray synchrotron microtomography were performed at the TOMCAT beamline of the Swiss Light Source [41]. The sample is probed by X-ray beam tuned to 20 keV using a double crystal multilayer monochromator. 2160 projections were recorded in absorption mode using 16 bit PCO.edge CMOS detector coupled with a 40X optical magnifying lens to a 5.9 micrometer thick LSO:Tb scintillator. The observed region is cuboid in shape, with dimensions 265 µm × 265 µm × 160 µm, and isotropic voxel size of 160 x 160 x 160 nm^3. Intermetallic particles and cavities observed in the reconstructed volume were segmented by manual thresholding. Labelling and parameters measurement was then performed using a dedicated image processing plugin implemented in ImageJ [42].

The shape and the orientation of the particles are defined based on the best-fitting ellipsoid with its three semi-axes R_1, R_2, R_3 ($R_1 \geq R_2 \geq R_3$). The particle aspect ratio W_p is defined as $W_p = R_1/\sqrt{R_2 R_3}$ and the orientation of the particle is defined by the angle between the major semi-axes R_1 and TD (see Fig. **1(a)**).

2.3. Uniaxial tensile tests

Uniaxial tensile tests were performed on a screw-driven universal machine under displacement control with 1 mm/min velocity. Cylindrical specimens, 4 mm in diameter, were machined along the FSP direction and along RD and TD for the base material (BM), see Fig. **1.(a)**. The initial gauge length was equal to 30 mm. The initial yield stress σ_0 is extracted from the stress-strain curves. The true fracture strain defined as $\varepsilon_f = \ln(A_0/A_f)$ is determined from broken specimens, with A_0 and A_f being respectively the initial and final cross-section area.

A number of tensile tests on specimens extracted from the BM and from the six passes FSPed material were interrupted prior to necking and polished down to mid-thickness along the transverse section in order to analyze the fraction of damaged particles. If the particle is broken, its surface is reconstructed by manually merging all fragments together. Approximately 2,000 particles have been analyzed for each interrupted test.

One interrupted tensile test of the BM loaded in RD and one of the FSPed material (6 passes) have also been characterized by microtomography. These tensile tests where both interrupted at a stress level of approximately 400 MPa. The samples have been extracted in the center of the specimens, see Fig. **2**. A method for reconstruction of broken particles observed within the 3D images is proposed in order to quantitatively study the fragmentation of each particle, see **Fig. 2**. After segmentation of the particles, a second segmentation of the cracks appearing in the broken particles was performed. These cracks are then dilated and any particles which are connected though a crack, i.e. particles which share at least one voxel with one same crack, were merged into a single particle. However it has only been possible to apply the reconstruction algorithm on the sample extracted from BM. Indeed, it was not possible to perform such segmentation for the broken particles in the FSPed material due to the very small size of the particles and hence, of their cracks.

3. Results and discussion

3.1. Intermetallic particles

Fig. **3** shows 3D perspective of intermetallic particles as observed by microtomography[1]. The volume fraction of particles F_p is always ~0.5 %. Indeed, FSP breaks-up the intermetallic particles but does not dissolve them. The BM contains some very large particles and the particles are preferentially aligned with RD. After 1 FSP pass, some large particles still remain intact but their spatial distribution is modified. After 3 and 6 passes of FSP, the mean particle size is clearly reduced and the spatial distribution gets more homogeneous.

3.1.1 Intermetallic particles size, shape and orientation

Fig. **4** presents the cumulative size distribution (volume-weighted) for the intermetallic particles based on 3D X-ray microtomography images (see section ***2.2***) as a function of the number of FSP passes (N_{FSP}). The equivalent diameter D_{eq} corresponds to the diameter of a sphere with the same volume as the particle. The fracture and abrasion of large brittle particles is known to depend on the nature of the pre-existing flaws in these particles and thus on their volume, since the largest defects are more likely to be found in the largest particles [**6**,**43**]. The stress level within the particle depends on the flow stress of the matrix, on the aspect ratio of the particles W_p [**44**] as well as on the local particle volume fraction (due to cluster-induced stress concentration [**45**]).

Figure **5(a)** presents the volume-weighted aspect ratio distribution of the particles. FSP breaks the large particles into smaller and more rounded fragments; i.e. the proportion of particles with an aspect ratio close to one increases with N_{FSP}. This trend is explained by Figure **5(b).** In the BM, the coarse particles are more elongated, i.e. D_{eq} increases with W_p. Since the large particles are more likely to contain defects, they are more prone to break and the proportion of elongated particles decreases with increasing N_{FSP}. Fig. **5(c)** and Fig. **5(d)** illustrate that the large and elongated particles in the BM tend to align along RD, i.e. have an angle close to 90° with TD. Again, since these large particles are more prone to break, this preferred orientation

[1] The color code will be explained later and can be ignored at present time.

is progressively eliminated with the increase of FSP passes. A minimum of 3 passes of FSP is required to generate significant changes.

3.1.2 Spatial distribution of intermetallic particles

a) Short-range neighboring

A 3D ‘‘finite body’’ tessellation [**46,47**] was applied on the microtomography images in order to quantify the spatial distributions of the particles (voids are excluded). Indeed, a more classical Voronoi tessellation based only on the centroids of the particles is not well suited for particles with irregular shapes [**46**]. The finite body tessellation consists in the following procedure: (i) segmentation by thresholding and labelling of the particles, (ii) computation of the 3D Euclidean Distance Map (EDM), (iii) computation of the 3D watershed from the EDM. The procedure is illustrated in 2D in Fig. **6(a-c)** for clarity and its result is shown in 3D in Fig. **6(d).** It results in a network of cells such that every point within a cell is closer to the corresponding particle than to any other [**46,47**].

Indicators of the distribution homogeneity are computed based on post-processing of the tessellated cells. The local volume fraction F_p^{local} is defined as the ratio of the particle volume to the volume of its associated cell. Neighbors are defined as the particles associated with cells that directly share one face with the cell of the given particle. The nearest-neighbor d_{nn} and near-neighbor d_n distances can then easily be calculated as respectively the minimum and mean distance between the particle and all neighbors.

The line entitled ‘All particles” in **Table 1** compares the mean F_p^{local} of all cells. The standard deviation of F_p^{local} for all particles is given also as an indicator of the degree of homogeneity of the distribution **[48]**. As expected, the mean value of F_p^{local} is close to 0.5% in each case, i.e. similar to the global volume fraction. Indeed, FSP breaks-up the intermetallic particles but does not dissolve them and the global volume fraction remains unchanged. If compared with BM, the standard deviation of F_p^{local} is slightly higher for one pass of FSP and

then reduced for 3 and 6 passes. This is a first indication that the degree of clustering is reduced by FSP, but only after a minimum of 3 passes.

Figure **7** gives the distribution of d_{nn} and d_n as a function of N_{FSP}. All distances given in the following analysis correspond to true particle spacing (the size of the ligament of matrix), i.e. the minimum Euclidian distance between two voxels from each particle, and not the distance from centroid to centroid. Section ***3.1.1*** demonstrated that large intermetallic particles are fragmented by successive FSP passes. It means that the number of particles per unit volume ρ increases and thus that the mean distance between particles decreases. In order to compare the homogeneity of the distribution on a relative basis, the measured distances have been normalized by a factor $\rho^{-\frac{1}{3}}$. The "occurrence" is calculated as the ratio of the population in the class divided by the total number of particles. The distribution of d_{nn} in BM shows that a lot of particles have at least one neighbor in very close proximity. This corresponds to particles located within a cluster. On the opposite side of the distribution, a small fraction of particles are quite distant from all their neighbors. This corresponds to isolated particles. As N_{FSP} increases, more and more particles have a normalized d_{nn} around 0.5. As detailed by Chandrasekar [**49**], the expected normalized d_{nn} in a perfectly random distribution of particles should be equal to 0.554. This indicates that the distribution of particles gets closer to a random distribution when N_{FSP} increases. The distribution of d_n (see Fig. **7**.(b)) shows that in the BM and after one FSP pass, a large proportion of particles have a mean normalized distance to their neighbors significantly smaller or significantly larger than one. Again, this corresponds respectively to particles outside and within clusters. After three and six FSP passes, the distribution becomes more homogeneous.

b) Clustering analysis

In order to understand the influence of clusters on the damage evolution, one should be able to distinguish clusters from the isolated particles [**50,51**]. An analysis proposed by Achon *et al*

[52] was used here to further characterize the clusters within the 3D particle field observed by microtomography (see supplementary material for more details on Achon's method). A particle is assumed to belong to a cluster if all of near-neighbors identified from the tessellated particle field are within a distance $d_{Cluster}$ or less. The distance $d_{Cluster}$ should be an objective characteristic of the particles spatial distribution. If the distance $d_{Cluster}$ increases, the number of clusters increases. At some point, the number of identified clusters starts to decrease because the distance $d_{Cluster}$ becomes so large that the clusters coalesce with one another. The "clustering distance" of the distribution selected here is the value of $d_{Cluster}$ corresponding to the maximum number of clusters identified within the particle field.

This procedure distinguishes isolated particles, i.e. particles that are distant from all their neighbors by a distance larger than $d_{Cluster}$, from particles belonging to clusters. However, some clusters contain a low number of particles and no physical meaning in the sense that they could be found in a random distribution of particles. These random clusters are identified in the following manner: each particle is randomly relocated within the analyzed volume, with no overlap allowed. The analysis is then performed on this random distribution with the selected clustering distance. The largest number of particles which belong to a similar cluster within the random distribution is defined as the minimum cluster size, i.e. the mean number of particles per cluster. In other words, any particle belonging to a cluster composed of fewer particles than the minimum cluster size is considered as isolated.

Table 2 summarizes the main indicators resulting from the clustering analysis carried out on the microtomography images. The selected clustering distance decreases with N_{FSP}. Indeed, more and more particles are fragmented and the number of particles per unit volume increases. The mean distance between particles decreases and the clusters start coalescing with each other for a smaller distance. The mean cluster size first increases for 1 FSP pass and then decreases for 3 and 6 passes compared to the BM. The percentage of particles within

clusters decreases with N_{FSP}. Note that the volume-weighted percentage of particles within clusters is higher than the number-weighted percentage in every case. This means that the large particles tend to be more clustered. These large particles are more prone to fragmentation and this will contribute to the reduction of clustering. The analysis differentiate isolated particles from particles within clusters, and the mean local particle volume fraction F_p^{local} of cells which belong to clusters compared to those of isolated particles is given in **Table 1.** Clusters correspond to a higher F_p^{local} than isolated particles. The mean local particle fraction increases with N_{FSP} for isolated particles. Because the particle distribution is progressively homogenized and more and more cells have a F_p^{local} similar to the global value. The mean F_p^{local} within clusters increases after 1 FSP pass, in agreement with the increased size of clusters, as large particles found in the BM break into smaller fragments. However, the redistribution remains local and is not sufficient to displace them far away from the parent particles. These fragments contribute to increase the cluster length to which the parent particle belongs and increase F_p^{local} after one FSP pass.

c) Long-range neighboring

One drawback of the nearest neighbor analysis is that it places more emphasis on the nearby particles and ignores the longer range characteristics of the arrangement. A classical way to analyze medium to large particles spacing is to use the radial distribution function (*RDF*), i.e. the probability for a neighboring particle to be located at a distance *r*, in any direction [**53**]. However, clusters in the BM exhibit anisotropic shape with particles preferentially aligned in the RD. As a consequence the *RDF* analysis needs to be modified in order to take into account both distance and angular dependence of the particles spacing. The extended pair correlation function (PCF) already proposed in Refs. [**53,54**] is slightly modified here and directly applied to the 3D X-ray microtomography images. The PCF function is defined, in 3D, as the probability for a given point [x,y,z] to be located inside a particle, given that another particle

is located at the origin [0,0,0]. **Fig. 8** shows how the PCF function can be calculated for a 3D volume extracted from the BM. The procedure is described in the supplementary material.

For a perfectly homogeneous spatial distribution, the PCF would be equal to 1 for each point. A PCF value smaller or larger than 1 corresponds thus respectively to a smaller or larger probability to find a neighbor in the vicinity of a particle compared to a perfectly homogenous distribution. The origin in the PCF plots is at the center and has a value equal to 0 because the point has to fall in a neighboring particle and not in the reference particle.

In order to interpret the PCF, Fig. **8(a)** shows the 2D cross-section through the center of the sub-volume in the plane RD-TD, TD-STD and RD-STD for the BM. The area with the highest PCF is parallel to the RD, due to the stringer-type clustering along RD, as already qualitatively observed. On the opposite, the PCF is observed to be smaller in the TD. Fig. **8(b)** shows the RD-TD cross-section as a function of N_{FSP}. FSP randomizes the particles distribution and make the spatial distribution of the particles in the material more isotropic. After one FSP pass, regions of space with high PCF are still observed, but the clustering is not anymore strongly oriented along the RD compared to the BM. This indicates that clusters of particles are still found after 1 FSP pass, but these clusters have a more isotropic shape. After 3 and 6 FSP passes, the PCF approximately ranges in the interval [0, 2] at each point of space, due to the strong declustering.

3.2. Initial porosity

Figs**. 9(a)** and **9(b)** respectively present the evolution of the volume fraction f_0 and mean equivalent diameter of the porosity initially present, i.e. prior to testing. The initial porosity originates from intermetallic particles fracture during the rolling process [**50**] (see Fig**. 9(c)**) or from the gathering, during Al solidification, of the hydrogen dissolved in liquid Al [**55**] (see Fig**. 9(d)**). FSP significantly reduces the porosity volume fraction (see Fig**. 9(a)**) and the mean equivalent diameter of the voids (see Fig**. 9(b)**). The closure of the cavities by FSP is

probably due to the complex nature of material flow and the high shear strain within the deformed zone [19]. The first steps of the closure of the void due to the material flow after 1 FSP pass is qualitatively presented in Fig**. 9(e)**.

3.3 Summary about microstructural evolution upon FSP

The physical scenario schematically illustrated in Fig. **10** emerges from the microstructural characterization presented in the sections *3.1 and 3.2*:

(i) In the BM, intermetallic particles are preferentially aligned along RD and this results in a stringer-type clustering. The coarse particles are the most elongated.

(ii) After one FSP pass, the largest (also elongated) particles are broken into smaller fragments but the redistribution of these fragments remains local. The fragments remain within the cluster to which the parent particle belongs with no reduction of the degree of clustering. However, this local redistribution is sufficient to mitigate the preferred orientation for particle clustering. The aspect ratio of the large intermetallic particles is decreased by FSP due to their breakage perpendicular to their long dimension.

(iii) After 3 FSP passes, the decrease of particle size progressively saturates. This saturation is due to the fact that the small broken fragments become very difficult to break. The fragments get more homogeneously distributed and the degree of clustering is reduced.

(iv) Performing more than 3 FSP passes (i.e. 6 FSP passes) provides little improvement in size reduction and homogenization of the distribution.

(v) FSP also reduces the initial porosity owing to the extreme applied deformation.

3.4. Uniaxial tensile tests

3.4.1 Interrupted tensile tests

Fig. 11(a) shows the true stress-true strain response of the BM in T4 state in RD and TD, as well as of a FSPed sample after 1h at 180°C of heat treatment. This last heat treatment condition has been selected because it provides almost the same hardening behavior as the T4

BM, hence allowing comparisons of the damage evolution at similar stress levels. The BM exhibits weak plastic anisotropy. Each point on the curves corresponds to a tensile test interrupted prior to necking in order to limit the growth of nucleated voids and to facilitate reconstruction of the broken particles (see *section 2.3).* The variation of the fraction of damaged particles measured on polished cross-sections is given in Fig. **11(b)** as a function of the applied stress. Particle fracture is the dominant nucleation mechanism in BM. For the same macroscopic stress, the fraction of broken particles in BM is significantly higher when loaded along the RD. Indeed, as discussed in *section 3.1.1*, particles are elongated and preferentially aligned along RD, which increases the load transfer arising from the deformation mismatch between the particle and matrix [**44**]. Furthermore, for the same stress, the fraction of damaged particles drops in the FSPed material. The large and most brittle particles in the BM have been broken into smaller and more resistant fragments in the FSPed material. Void nucleation by interface decohesion is now observed in the 6 passes FSPed material for some particles (12% to 19% of the damaged particles when the stress increases from 353 MPa to 398 MPa). This could be due to a degraded interface between the fragments and the matrix formed during FSP. It is also likely that because the remaining fragments are the strongest parts of the particles, these are more and more difficult to break. However, particles fracture remains the main nucleation mechanism indicating that for a majority of fragments the adhesion with the matrix remains high.

As explained in *section 2.3*, reconstruction of the broken particles has only been possible on the microtomography images of the BM. Micrographs of the BM and FSPed samples are given in **Fig. 11(c)** for qualitative analysis only. The loading direction corresponds to RD. Large particles preferentially aligned with RD are found within the BM broken perpendicularly to the loading direction, at more than one location. In the FSPed material, the intermetallic particles are smaller and quite homogeneously distributed within the matrix. The

fraction of broken particles is much lower compared to BM and the cracks are formed in the few larger particles not fragmented by FSP, as indicated by arrows in **Fig. 11(c)**.

Figure **2** shows a sub-volume extracted from the tomographic volume of BM (loaded in RD up to 420 MPa) obtained after automatized particle reconstruction, see section 2.3. Unbroken particles are in blue. Fig. **12(a)** shows the fraction of broken particles as a function of the reconstructed particles size, obtained from both SEM analysis and microtomography. The differences between the two techniques are probably due to the difference of ratio between resolution and feature size and to the fact that the particles are not perfectly equiaxed. However, the trends are the same. The microtomography analysis shows that particles with D_{eq} < ~1µm are almost never damaged while particles with D_{eq} > ~5µm are almost always broken. Fig. **12(b)** also shows that while most of the particles with D_{eq} < ~3µm crack only once, the number of cracks increases with particle size. This indicates that the very large particles, i.e. larger than ~ 3-4 µm, are the most detrimental as they tend to break into multiple fragments. As shown in Fig. **4,** the fraction of these large particles is highly reduced after six FSP passes and this strongly reduces the volume fraction of nucleated voids [**6**].

3.4.2 Fracture strain

Figure **13**(a) shows, for the BM and for the FSPed material, the variation of the fracture strains (ε_f) as a function of σ_0 corresponding to the various heat treatments. First, ε_f of BM when deformed along RD are compared with ε_f after 3 and 6 FSP passes along RD. For the same σ_0, ε_f is significantly larger in the FSPed material. For the sake of a better physical appraisal of the difference, Fig **13(b)** presents the same data in terms of engineering strain. It is remarkable that ε_f in TD is doubled after 6 passes. In the LD, ε_f is improved by 20%. This is clearly due to the fact that FSP breaks the large intermetallic particles into smaller and thus stronger fragments *(see section 3.1.1 and Fig. **12**)*, that FSP closes the existing initial porosity

*(see section 3.2 and Fig. **9**)* and that FSP reduces the degree of clustering *(see section 3.1.2, Table 1, Table 2 and Fig. **8**).*

While relatively low plastic anisotropy was observed (see section 3.4.1 and Fig. **11.(a)**), the anisotropy in ε_f is significant in BM : ε_f is larger by about 0.2 in RD compared to TD. The tessellation analysis on BM revealed that the majority of cells are elongated in RD, indicating that particle clustering is stronger along RD *(see section 3.1.2)*. Furthermore, the PCF analysis emphasized a stringer-type clustering along RD, providing an easy percolating crack path when loading in TD which is likely to lower ε_f. A higher fraction of broken particles was observed in BM when loaded along RD, which would be associated with a lower ε_f. This means that the effect of particle spatial distribution on coalescence is the dominant parameter setting the anisotropy in the BM. After 6 FSP passes, the anisotropy in ε_f is suppressed. This is in agreement with the PCF and tessellation analysis, from which it was concluded that FSP randomizes the distribution after a minimum of 3 FSP passes.

After 1 FSP pass along RD, ε_f decreases compared to BM when deformed along RD. Indeed, a lot a large particles (i.e larger than about 3 μm) are still present after 1 FSP pass (see Figure **4**). Void nucleation is thus not expected to be significantly postponed. The fact that ε_f even decreases compared to BM can be explained based on the PCF analysis (see **Fig. 8**). Indeed, when deforming BM along RD, the coalescence process is likely to be postponed since the PCF is lower than the one along TD. However, after 1 FSP pass, the anisotropy of the PCF decreases and the coalescence process will be faster.

4. Damage model

An elementary 3D damage model is proposed in order to semi-quantitatively uncouple the effect of particle size and particle spatial distribution. The X-ray tomography images of the

BM and FSPed material (see Fig. **3**) are used as representative volume element (RVE), involving the positions (x_i,y_i,z_i) and the dimensions of the particles. The particles are assumed to be ellipsoidal, with main semi-axes R_1, R_2 and R_3 ($R_1 \geq R_2 \geq R_3$) respectively aligned with RD, TD and STD, see ***section 3.1***. The RVE is a cube of 160 µm side, which corresponds to a particle field ranging between approximately 4,000 particles in BM up to approximately 14,000 particles after 6 FSP passes. The model is applied for the T4 state only, exploiting the experimental data of the interrupted tensile tests (see *section 3.4.1*). The initial yield stress σ_0, the uniform strain ε_u and the strain hardening parameters are extracted from the true stress–strain curve (in T-direction only) based on an extended Voce law, see Ref. **[6].** The same hardening parameters are used in all cases, i.e. neglecting any plastic anisotropy or effect of FSP on the plastic flow behavior (see Fig. **11(a)**). The presence of an initial porosity f_0 facilitates void linkage and accelerates ductile failure. However, this effect is attenuated for a hard matrix (T4 and T6 state) compared to a soft matrix (over-aged state). Indeed, void nucleation is more significant for particles surrounded by a hard matrix, attenuating the impact of f_0 [6]. The effect of f_0 is thus also neglected in the present analysis focused on the T4 state, see Ref. [6] for a more advanced model.

The fraction of broken particles $P(\sigma_y,V_{mean})$ is assumed to be a function of the flow stress σ_y and of the average particle size V_{mean}. The possible effects of particle size distribution (i.e. the scatter around the mean value) and particle orientation on the nucleation rate are neglected. The experimental fraction of broken particles in the interrupted tensile tests (see Figure **11(b)**) is then fitted using the following probability function :

$$P(\sigma_y, V_{mean}) = 1 - \exp\left(-K_1\, V_{mean}\, (\sigma_y)^{K_2}\right) \qquad (1)$$

where V_{mean} is the only parameter that depends on N_{FSP}, i.e. the same nucleation stress distribution versus particle size is used. A reasonable fit of the broken particle fraction for the BM and 6 FSP passes (see Fig. **14**) is obtained with K_1=3.17e^{-9} and K_2 = 2.7. The anisotropy

of void nucleation in BM remains limited and the same nucleation law gives an acceptable fit for both loading directions. The nucleation process is cumulative and can be seen as a nucleation front moving through the particle size distribution **[56]**. In other words, for a given fraction of broken particles $P(\sigma_y,V_{mean})$, voids nucleate on particles larger than a critical size V_{crit}. V_{crit} corresponds to the threshold size for which a fraction $P(\sigma_y,V_{mean})$ of particles are larger than V_{crit}. Fig. **14** shows that for a given applied stress, the fraction of broken particles decreases with N_{FSP} due to particle size reduction.

The nucleated void is assumed to appear in the middle of the particle and is given by the intersection of the 3D particle with a plane perpendicular to the loading direction. The equivalent radius R_{eq} of the void corresponds to the radius of a circle with the same area as the particle intersection. Void growth is modelled using the Rice and Tracey [57] isotropic void growth analysis corrected by Huang [58]:

$$\frac{dR_{eq}}{R_{eq}} = 0.427\, T^{0.25} \exp\left(\frac{3}{2}T\right)\, d\varepsilon \qquad (2)$$

where ε is the effective plastic strain and T is the stress triaxiality given by T=1/3 (for $\varepsilon<\varepsilon_u$) and T = 1/3+0.41(ε-ε_u) (for $\varepsilon>\varepsilon_u$), with ε_u the uniform strain [59].

The Thomason's criterion [60] is used to predict void coalescence and is evaluated for each cavity with all its near-neighbors:

$$\frac{\sigma_n}{\sigma_0} = \left(1-\chi_{eff}^2\right)\left(0.1\left(\frac{1-\chi_{eff}}{\chi_{eff}}\right)^2 + 1.2\frac{1}{\sqrt{\chi_{eff}}}\right) \qquad (3)$$

where σ_n is the stress component normal to the ligament between the voids and χ_{eff} is the effective void spacing. For simplification, the void aspect ratio used in eq. (**3**) is taken equal to 1 (i.e. the two voids are supposed to be spherical) since this assumption was shown in a previous study [6] to have a limited effect on the value of ε_f for this ductile Al alloy. Indeed, a significant amount of void growth occurs before the coalescence criterion is fulfilled. When this happens, the void shape is always close to equiaxed. The overall stress component normal

to the ligament σ_n is approximated by $\sigma_n = \sigma_y \sin(\alpha)^2$, with α the angle between the ligament and the loading direction. The effective void spacing χ_{eff} is given by:

$$\chi_{eff} = \frac{R_{eq}^1 + R_{eq}^2}{L_{1-2}} \quad (4)$$

where $L_{1\text{-}2}$ is the distance between void centers and R_{eq}^1 and R_{eq}^2 are the mean radii.

The ratio of the number of cavities satisfying the coalescence criterion over the total number of particles is an indication of the number of microcracks developing within the material. The evolution of this ratio is shown in Figure **15**(a) as a function of the applied strain, orientation and N_{FSP}. The vertical lines indicate the experimental ε_f. A ratio of **10%** of microcracks compared to the number of particles corresponds reasonably well with the experimental ε_f (see Fig. **15(a)**). If this critical ratio is chosen as an empirical fracture criterion, the model captures the anisotropy on ε_f for BM. Furthermore, the model predicts isotropic ε_f after 6 FSP passes, owing to the particle distribution randomization (see section 3.2 and Figure **8**). The results of the model for 1 FSP pass indicates a limited improvement of ε_f compared to the BM, in good agreement with the experiments. In the case of 3 FSP passes, ε_f is significantly larger due to highly reduced particle size (see section 3.1.1). After 6 FSP passes, ε_f is not much improved because of particle size saturation (see Figure **4**) and the similar spatial distribution after 3 and 6 FSP passes (see section 3.2).

This model allows decoupling the effect of the void size on nucleation and of the spatial distribution on coalescence. Indeed, if the mean size V_{mean} in eq. (***1***) is kept constant and equal to the value of BM (*i.e.* if all samples have the nucleation law given by the red curve in Fig. **14**), the effect of the particle size on void nucleation is not taken into account. Any change in ε_f is then related to the particle spatial distribution only. Results of the model without the size effect on void nucleation are provided in Fig. **15**(b). Without the effect of particle size on the

void nucleation, ε_f of the FSPed samples remains between ε_f of BM along RD and TD. Without FSP, the clustering alignment along RD explains the low value of ε_f in TD. This effect disappears after FSP. This analysis shows that the improvement of ductility with N_{FSP} is mainly due to the delay on void nucleation owing to the reduction of particle size.

5. Conclusions

Friction stir processing (FSP) has been performed on a 6056 rolled Al alloy. Detailed analysis of 3D high resolution X-ray synchrotron tomography data of the BM and FSP after 1, 3 and 6 FSP passes have provided the following information:

• The intermetallic particle size decreases with the number of FSP passes.

• The large intermetallic particles are also initially more elongated and are rounded up by FSP due to their breakage by the large deformations involved in the process.

• FSP homogenizes the particle distribution, as quantitatively demonstrated by the tessellation, clustering and pair correlation functions analyses.

• The initial porosity present in the BM is first reduced in size and then suppressed by an increasing number of FSP passes.

• A simple FSP pass is not sufficient to ensure the full potential of the process to break the intermetallic particles and to homogenize their distribution.

Tensile testing and interrupted tensile tests of BM and FSPed samples have provided the following key results:

• The fracture strain of FSP samples is improved by almost 100% in the best cases compared to the BM tensile samples at identical yield strength.

• The nucleation stress for the fracture of intermetallic particles (i.e. the source of damage in these alloys) increases in the FSP samples.

• Friction stir processing leads to an isotropic fracture behavior.

A simple damage model has been used to uncouple the effect of particle size and spatial distribution. The homogenization of the particle distribution is the main reason for the isotropy of the FSPed material. The reduction in size of the intermetallic particles, retarding void nucleation, explains the improvement of the damage resistance of the FSPed samples. Void nucleation retardation has been quantitatively characterized based on ex situ tensile test in X-ray microtomography. Earlier works have shown that miniature tensile specimens can be used to determine the mechanical and fracture properties of the weld [**61,62**]. Future work will consider in situ tensile testing of such miniature specimens in order to quantitatively characterize the evolution of the damage process. It will allow validating the effect of FSP on void nucleation and gain insight on its impact on the void growth and the coalescence process.

Acknowledgements
The authors would like to thank SLS for the attribution of beam time on the TOMCAT beamline. The authors acknowledge the financial support of the Interuniversity Attraction Poles Program from the Belgian State through the Belgian Policy agency, contract IAP7/21 INTEMATE. F. Hannard acknowledges the financial support of FRIA, Belgium. The collaboration between UCL and INSA-Lyon is financed by a Tournesol 2013 project.

References
[**1**] Puttik K, Ductile fracture in metals, Phil. Mag. 4 (1959) 964–969.
[**2**] G. Çam, M. Koçak, Microstructural and Mechanical Characterization of Electron Beam Welded Al-Alloy 7020, J. Mater. Sci. 42 (17) (2007) 7154-7161.
[**3**] G. Çam, M. Koçak, D. Dobi, L. Heikinheimo, M. Siren, Fracture Behaviour of Diffusion Bonded Bimaterial Ti-Al Joints, Sci. Technol. Weld. Join. 2 (3) (1997) 95-101.
[**4**] A. Simar, K.L. Nielsen, B. de Meester, V. Tvergaard, T. Pardoen, Micro-mechanical modelling of ductile failure in 6005A aluminium using a physics based strain hardening law including stage IV, Engin. Fract. Mech. 77 (13) (2010) 2491-2503.
[**5**] A. Simar, Y. Bréchet, B. de Meester, A. Denquin, C. Gallais, T. Pardoen, Integrated modelling of friction stir welding of 6XXX series aluminium alloys: process, microstructure and properties, Progress Mater. Sci. 57 (2012) 95-183.
[**6**] F. Hannard, T. Pardoen, E. Maire, C. Le Bourlot, R. Mokso, A. Simar, Characterization and micromechanical modelling of microstructural heterogeneity effects on ductile fracture of 6xxx aluminium alloys, Acta Mater 103 (2016) 558-572.
[**7**] S.H. Goods, L.M. Brown, The nucleation of cavities by plastic deformation, Acta Metall 27 (1979) 1–15.
[**8**] L. Babout, E. Maire, R. Fougres, Damage initiation in model metallic materials:

X-ray tomography and modelling, Acta Mater 52 (8) (2004) 2475–2487.
[9] Z. Chen, C. Butcher, Application of the complete percolation model, in: Micromechanics Modelling of Ductile Fracture, Vol. 195, Solid Mechanics and its Applications, Springer, Netherlands, 2013, pp. 275–290.
[10] W.D. Lockwood, B. Tomaz, A.P. Reynolds, Mechanical response of friction stir welded AA2024: experiment and modeling, Mater. Sci. Engin. A 323(1) (2002) 348–353.
[11] C. Gallais, A. Denquin, Y. Bréchet, G. Lapasset, Precipitation microstructures in an AA6056 aluminium alloy after friction stir welding: Characterisation and modelling, Mater. Sci. Engin. A 496 (1–2) (2008) 77-89.
[12] S.R. Sharma, Z.Y. Ma, R.S. Mishra, Effect of friction stir processing on fatigue behavior of A356 alloy, Scripta Mater 51 (2004) 237–241.
[13] R.S. Mishra, P.S. De, N. Kumar, Friction Stir Welding and Processing, Science and Engineering, Springer, New York, 2014.
[14] G. Çam, S. Mıstıkoğlu, Recent Developments in Friction Stir Welding of Al-Alloys, J. Mater. Eng. Perform. 23 (6) (2014) 1936-1953
[15] G. Çam, Friction Stir Welded Structural Materials: Beyond Al-Alloys, Int. Mater. Rev. 56 (1) (2011) 1-48
[16] R.S. Mishra, Z.Y. Ma, Friction stir welding and processing, Mater. Sci. Eng. R-Rep. 50 (1–2) (2005) 1-78.
[17] Xiaocong He, Fengshou Gu, Andrew Ball, A review of numerical analysis of friction stir welding, Progress Mater. Sci. 65 (2014) 1-66.
[18] W.M. Thomas, E.D. Nicholas, J.C. Needham, M.G. Murch, P. Templesmith, C.J. Dawes. GB patent application no. 9125978.8, December 1991; US patent no. 5460317, October 1995.
[19] T. Long, W. Tang, A.P. Reynolds, Process response parameter relationships in Al alloy friction stir welds, Sci. Technol. Weld. Join. 12 (2007) 311-317.
[20] A.G. Rao, R.R. Ravi, B. Ramakrishnarao, V.P. Deshmukh, A. Sharma, N. Prabhu, B.P. Kashyap, Recrystallization phenomena during friction stir processing of hypereutectic aluminum-silicon Alloy, Metall. Mater. Trans. A 44 (2013) 1519-1529.
[21] N. Kumar, R.S. Mishra, Ultrafine-grained Al-Mg-Sc alloy via friction stir processing, Metall. Mater. Trans. A 44 (2013) 934-944.
[22] K.A.A. Hassan, A.F. Norman, D.A. Price, P.B. Prangnell, Stability of nugget zone grain structures in high strength Al-alloy friction stir welds during solution treatment, Acta Mater. 51(7) (2003) 1923-1936.
[23] I. Charit, R.S. Mishra, Abnormal grain growth in friction stir processed alloys, Scripta Mater. 58(5) (2008) 367-371.
[24] S. Jana, R.S. Mishra, J.A. Baumann, G.J. Grant, Effect of process parameters on abnormal grain growth during friction stir processing of cast Al alloy, Mater. Sci. Engin. A 528 (2010) 189-199.
[25] M.L. Santella, T. Engstrom, D. Storjohann, T.Y. Pan, Effects of friction stir processing on mechanical properties of cast aluminium alloys A319 and A356, Scripta Mater. 53 (2005) 201-206.
[26] Z.Y. Ma, S.R. Sharma, R.S. Mishra, Microstructural modification of as-cast Al-Si-Mg alloy by friction stir processing, Metall. Mater. Trans. A 37 (2006) 3323-3335.
[27] Z.Y. Ma, S.R. Sharma, R.S. Mishra, Effect of multi-pass friction stir processing on microstructure and tensile properties of a cast aluminium-silicon alloy, Scripta Mater. 54 (2006) 1623-1626.
[28] Z.Y. Ma, S.R. Sharma, R.S. Mishra, Effect of friction stir processing on the microstructure of cast A356 aluminium, *Mater. Sci. Engin. A* 433 (2006) 269-278.

[29] Z.Y. Ma, A.L. Pilchak, M.C. Juhas, J.C. Williams, Microstructural refinement and property enhancement of cast light alloys via friction stir processing, Scripta Mater. 58 (2008) 361-366.
[30] A.H. Feng, B.L. Xiao, Z.Y. Ma, R.S. Chen, Effect of Friction Stir Processing Procedures on Microstructure and Mechanical Properties of Mg-Al-Zn Casting, Metall. Mater. Trans. A 40 (2009) 2447-2456.
[31] S. Jana, R.S. Mishra, J.A. Baumann, G.J. Grant, Effect of friction stir processing on microstructure and tensile properties of investment cast Al-7Si-0.6Mg alloy, Metall. Mater. Trans. A 41 (2010) 2507-2521.
[32] Z.W. Chen, F. Abraham, J. Walker, Tensile Fracture Behavior of Friction Stir Processed Al-7Si-0.3Mg Cast Alloy, Mater. Sci. Forum 706-709 (2012) 971-976.
[33] L. Karthikeyan, V.S. Senthilkumar, V. Balasubramanian, S. Natarajan, Mechanical property and microstructural changes during friction stir processing of cast aluminium 2285 alloy, Mater. Design 30 (2009) 2237-2242.
[34] M.-N. Avettand-Fènoël, A. Simar, R. Shabadi, R. Taillard, B. de Meester, Characterization of oxide dispersion strengthened copper based materials developed by friction stir processing, Mat. Design 60 (2014) 343-357.
[35] K. Nakata, Y.G. Kim, H. Fujii, T. Tsumura, T. Komazaki, Improvement of mechanical properties of aluminium die casting alloy by multi-pass friction stir processing, Mater. Sci. Engin. A 437 (2006) 274-280.
[36] S.R. Sharma, R.S. Mishra, Fatigue crack growth behavior of friction stir processed aluminum alloy, Scripta Mater. 59 (2008) 395-398.
[37] S. Jana, R.S. Mishra, J.B. Baumann, G. Grant, Effect of stress ratio on the fatigue behavior of a friction stir processed cast Al-Si-Mg alloy, Scripta Mater. 61 (2009) 992-995.
[38] S. Jana, R.S. Mishra, J.B. Baumann, G. Grant, Effect of friction stir processing on fatigue behavior of an investment cast Al-7Si-0.6Mg alloy, Acta Mater. 58 (2010) 989-1003.
[39] P. Cavaliere, Effect of friction stir processing on the fatigue properties of a Zr-modified 2014 aluminium alloy, Mater. Charact. 57 (2006) 100-104.
[40] Rasband, W.S., ImageJ, U. S. National Institutes of Health, Bethesda, Maryland, USA, http://imagej.nih.gov/ij/, 1997-2015.
[41] Stampanoni, M. *et al.* Tomographic hard xray phase contrast micro and nano imaging at tomcat. AIP Conference Proceedings 1266, 13–7 (2010).
[42] V. Boulos, L. Salvo, V. Fristot, P. Lhuissier, D. Houzet, Investigating performance variations of an optimized GPU-ported granulometry algorithm, 18th International European Conference on Parallel and Distributed Computing, Rhodes Island, Greece (2012).
[43] Y. Bréchet, J. Newell, S. Tao, J.D. Embury, A note on particle comminution at large plastic strains in Al-SiC composites, Scripta Mater. 28 (1) (1993) 47-51.
[44] F. Beremin, Cavity formation from inclusions in ductile fracture of A508 steel, Metall. Mater Trans. A 12 (1981) 723–731.
[45] M.N. Shabrov, E. Sylven, S. Kim, D.H. Sherman, L. Chuzhoy, C.L. Briant, A. Needleman, Void nucleation by inclusion cracking, Metall. Mater. Trans. A 35 (2004) 1745–1755.
[46] Boselli J, Pitcher PD, Gregson PJ, Sinclair I. Secondary phase distribution analysis via finite body tessellation. J Microsc. 195 (1999) 104–112.
[47] A.E. Scott, I. Sinclair, S.M. Spearing, M.N. Mavrogordato, W. Hepples, Influence of voids on damage mechanisms in carbon/epoxy composites determined via high resolution computed tomography, Compos. Sci. Technol. 90 (2014) 147-153.
[48] G. Burger, E. Koken, D.S. Wilkinson, J.D. EMBURY, The Influence of Spatial Distributions on Metallurgical Processes, In Advances in Phase Transitions, Pergamon Press (1988) 247-262.

[49] Chandrasekhar, S., Stochastic Problems in Physics and Astronomy, Rev. Mod. Phys., 15 (1943) 1-89.
[50] Jidong Kang, David S. Wilkinson, Dmitri V. Malakhov, Herdawandi Halim, Mukesh Jain, J. David Embury, Raja K. Mishra, Effect of processing route on the spatial distributions of constituent particles and their role in the fracture process in AA5754 alloy sheet materials, Mat Sci Eng A-Struct, 456 (1–2) (2007) 85-92.
[51] Yves J.M. Bréchet, Clusters, plasticity and damage: a missing link?, Mat Sci Eng A-Struct, 175(1–2) (1994) 63-69.
[52] Achon, P., Ph. D. Thesis, Ecole Nationale Superieure des Mines de Paris, France, 1994.
[53] Rollett, Anthony D., Lee, S.-B., Campman, R., Rohrer, G.S., Three-Dimensional Characterization of Microstructure by Electron Back-Scatter Diffraction, Annu. Rev. Mater. Res. 37 (2007) 627-658.
[54] K. Marthinsen, J.M. Fridy, T.N. Rouns, K.B. Lippert, E. Nes, Characterization of 3-D particle distributions and effects on recrystallization kinetics and microstructure, Scripta Materialia 39(9) (1998) 1177-1183.
[55] H. Toda, H. Oogo, K. Horikawa, K. Uesugi, A. Takeuchi, Y. Suzuki, M. Nakazawa, Y. Aoki, M. Kobayashi, The true origin of ductile fracture in aluminum alloys, Metall. Mater Trans. A 45 (2) (2014) 765–776.
[56] J.D. Embury, Plastic flow in dispersion hardened materials, Metall. Trans. A, 16A (1985) 2191-2200.
[57] J.R. Rice, D.M. Tracey, On the ductile enlargement of voids in triaxial stress fields, J. Mech. Phys. Solids 17 (3) (1969) 201–217.
[58] Y. Huang, The role of nonuniform particle distribution in plastic flow localization, Mech. Mater 16 (3) (1993) 265–279.
[59] E. Maire, S. Zhou, J. Adrien, M. Dimichiel, Damage quantification in aluminium alloys using in situ tensile tests in X-ray tomography, Eng. Fract. Mech. 78 (15) (2011) 2679-2690.
[60] P. Thomason, Ductile Fracture of Metals, Pergamon Press, 1990.
[61] C. Genevois, A. Deschamps, P. Vacher, Comparative study on local and global mechanical properties of 2024 T351, 2024 T6 and 5251 O friction stir welds, Mat. Sci. Eng. A 415 (15) (2006) 162-170.
[62] Cam, G.; Erim, S.; Yeni, Ç.; Koçak, M. Determination of mechanical and fracture properties of laser beam welded steel joints. Weld. J. 78 (6) (1999) 193–201.

Tables :

		Base Metal	1 pass of FSP	3 passes of FSP	6 passes of FSP
Mean local volume fraction F_p	All particles	0.40 ± 0.96 %	0.50 ± 1.1 %	0.46 ± 0.64 %	0.51 ± 0.63 %
	Particles within clusters	0.62 %	0.93 %	0.55 %	0.6 %
	Isolated particles	0.15 %	0.22 %	0.3 %	0.37 %

Table 1. Local volume fraction resulting from the finite body tessellation ("All particles") and the clustering analysis ("Particles within clusters" and "isolated particles").

		Base Metal	1 pass of FSP	3 passes of FSP	6 passes of FSP
Selected clustering distance : $d_{Cluster}$		6.4 µm	4.65 µm	4.3 µm	4.0 µm
Mean size of clusters		26 particles	35 particles	20 particles	15 particles
Percentage of particles within clusters	**volume-weighted**	67.2 %	61.4 %	32.2 %	15.6 %
	number-weighted	40.3 %	44.3 %	25 %	10.7 %

Table 2. Indicators resulting from the clustering analysis.

Figures

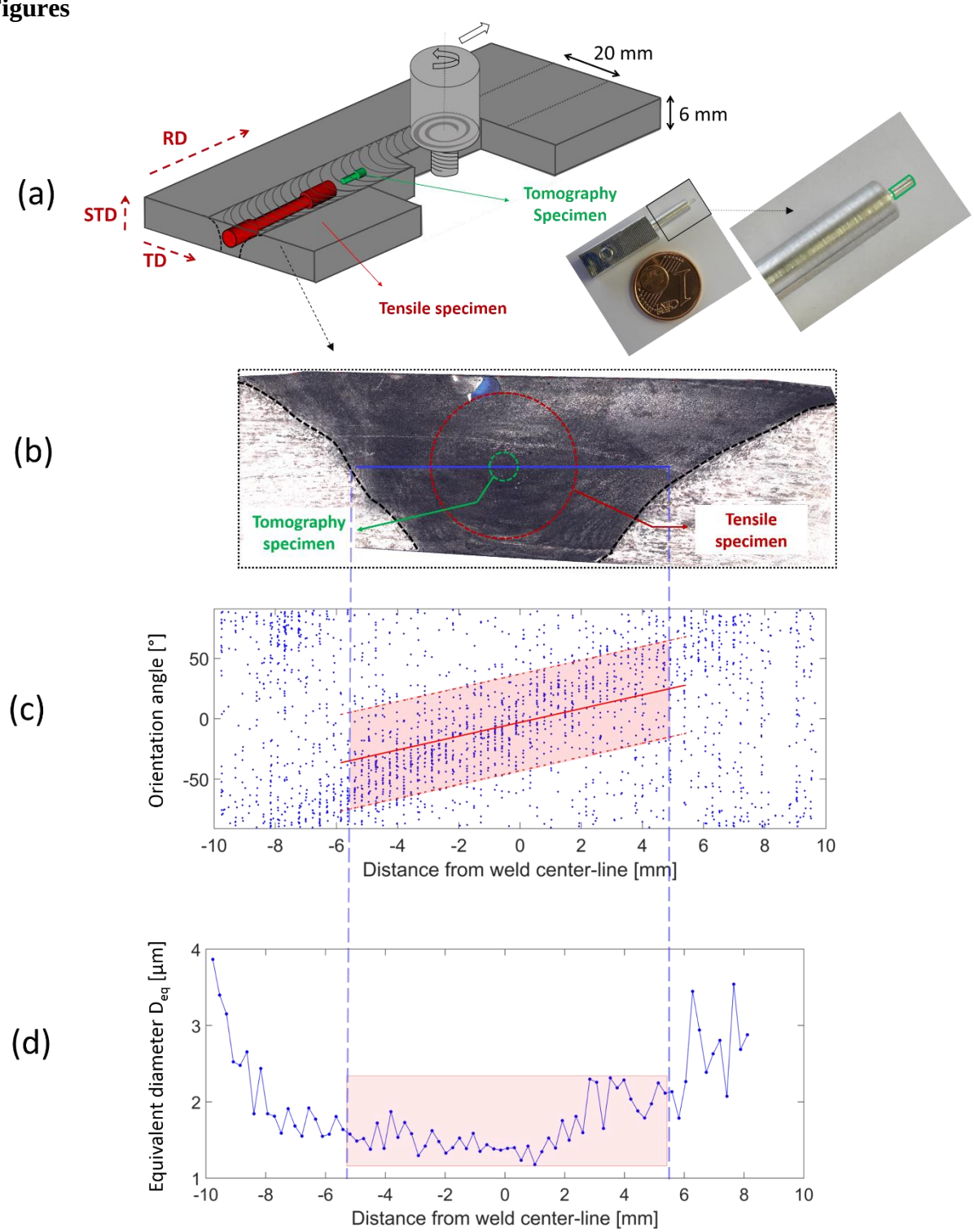

Figure 1. (a) Schematic of the FSP configuration and the geometry of extracted tensile and tomography specimens, (b) micrography of the cross-section of the weld in a plane perpendicular to the processing direction with visualization of the tensile (red) and tomography (green) specimens location, the SEM micrographs are taken in the RD-TD plane represented by the blue line in the cross-section. (c) Angle between the major axis of the particle and the transverse direction and (d) equivalent diameter of the particles observed on the SEM micrographs.

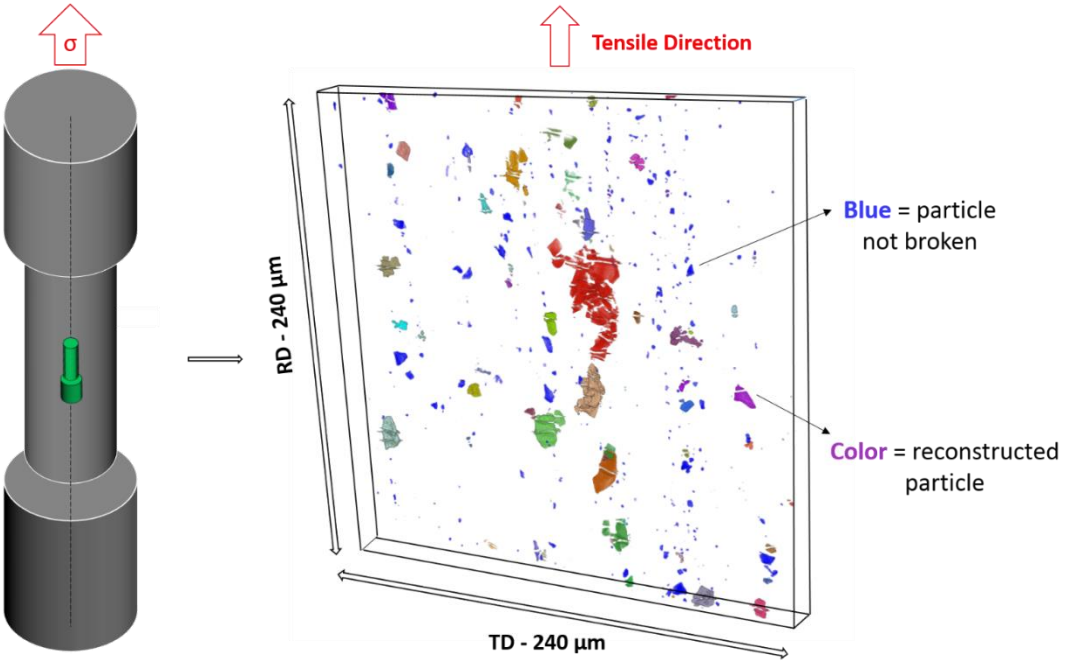

Figure **2**. Schematic of a tensile sample loaded in the RD up to 420 MPa (left figure) and visualization of a sub-volume (right figure) extracted from the total volume scanned by tomography in the base material after automatized particle reconstruction. The unbroken particles are in blue and the fragments corresponding to a fragmented and further reconstructed particle are shown with the other colors (one colour per particle).

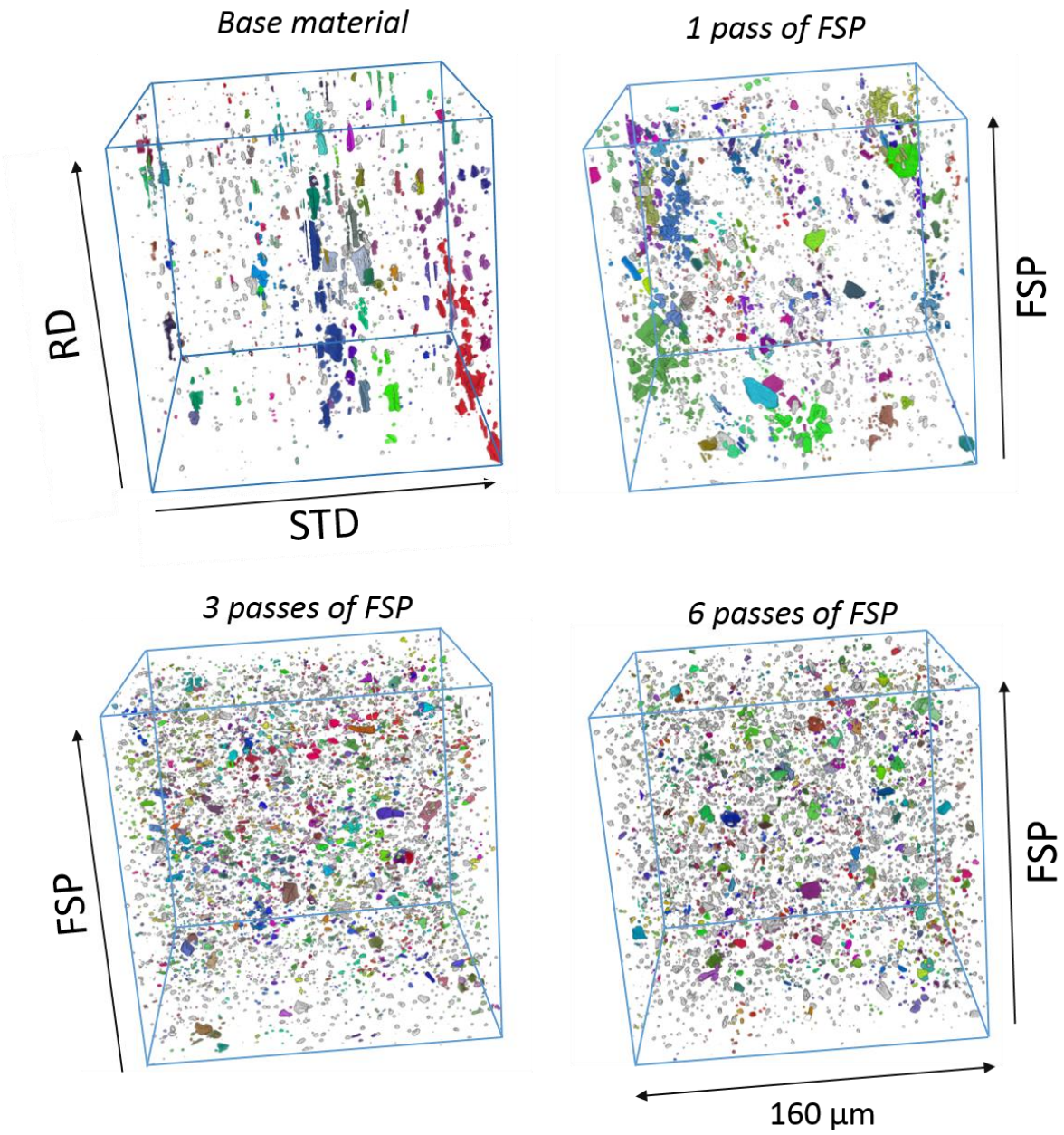

Figure 3. 3D microtomography perspectives of intermetallic particles distribution for the 6056 base material and for 1, 3 or 6 passes of FSP. White particles correspond to isolated particles, and particles with the same color belong to the same cluster according to the definition given in section 3.1.2. RD = rolling direction, STD = short transverse direction.

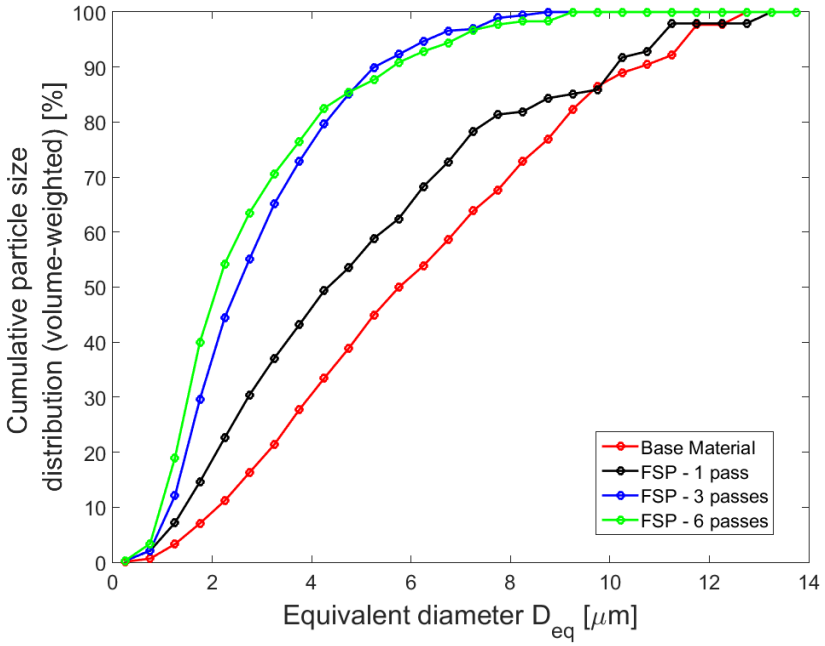

Figure **4**. Cumulative particle size distribution (volume-weighted) for the intermetallic particles based on the 3D X-ray microtomography images.

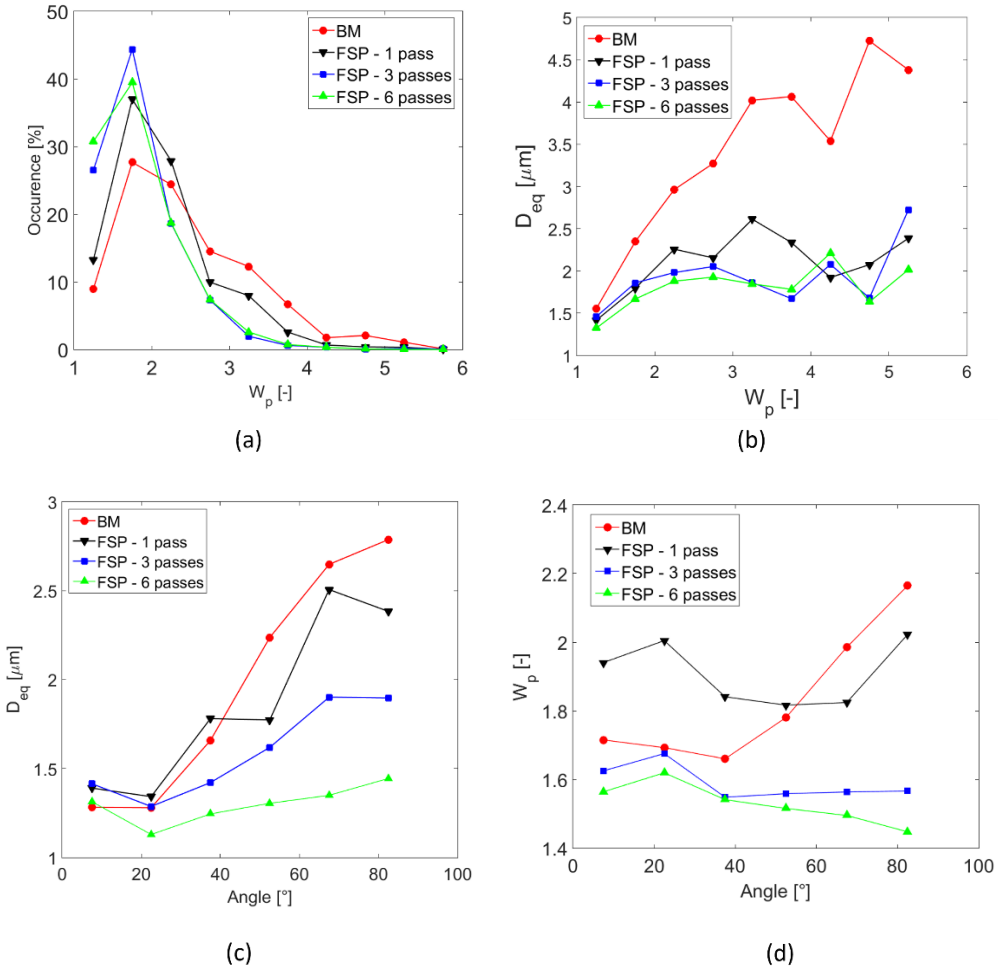

Figure **5**. Morphological parameters of the particles for different number of FSP passes: (a) Distribution of the aspect ratio; (b) Equivalent diameter (D_{eq}) as a function of the aspect ratio (W_p); (c) Equivalent diameter (D_{eq}) as a function of the angle between the major axis of the particle and the transverse direction (TD); (d) Aspect ratio as a function of the angle between the major axis of the particle and the transverse direction (TD). BM = base material.

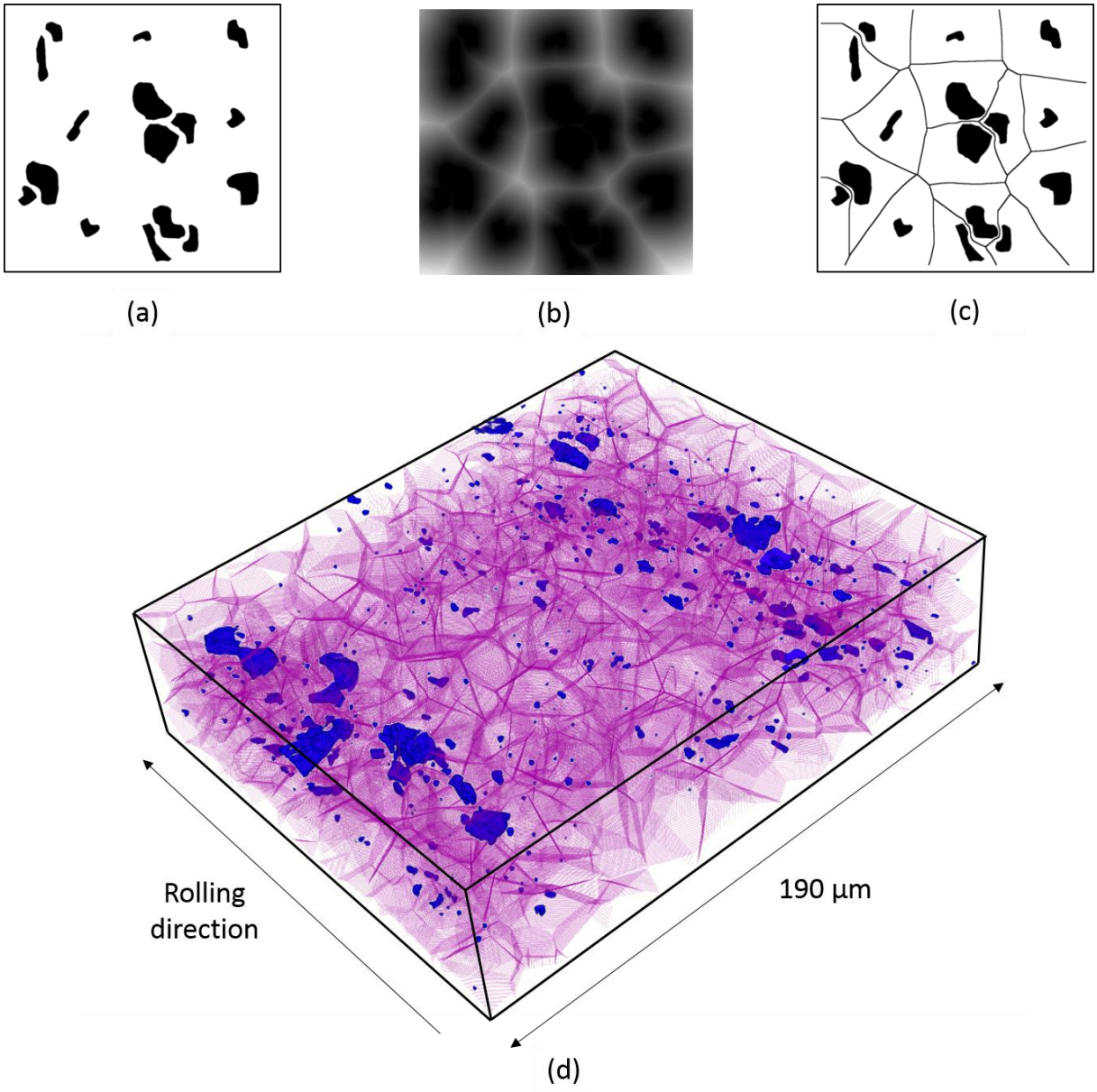

Figure 6 Example in 2D of the (a) segmented particles field, (b) distance map of the labelled particles with the distance visualized by greyscale, and (c) watershed cells and the particles superposed. (d) Visualization of the result of the procedure applied in 3D to a sub-box of the microtomography image of the base material where particles are in blue and cells are in purple.

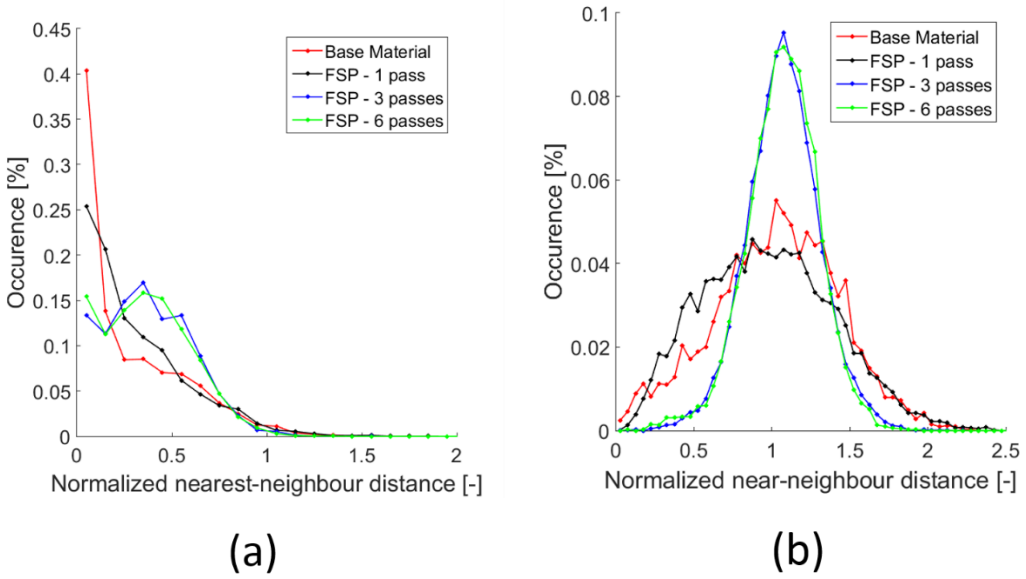

Figure 7. Distribution of (a) nearest-neighbour distances and (b) nearest-neighbour distances as a function of the number of FSP passes. Distances have been normalized by $\rho^{-1/3}$, with ρ the number of particles per unit volume. The "occurrence" is calculated as the ratio of the population in the class divided by the total number of particles.

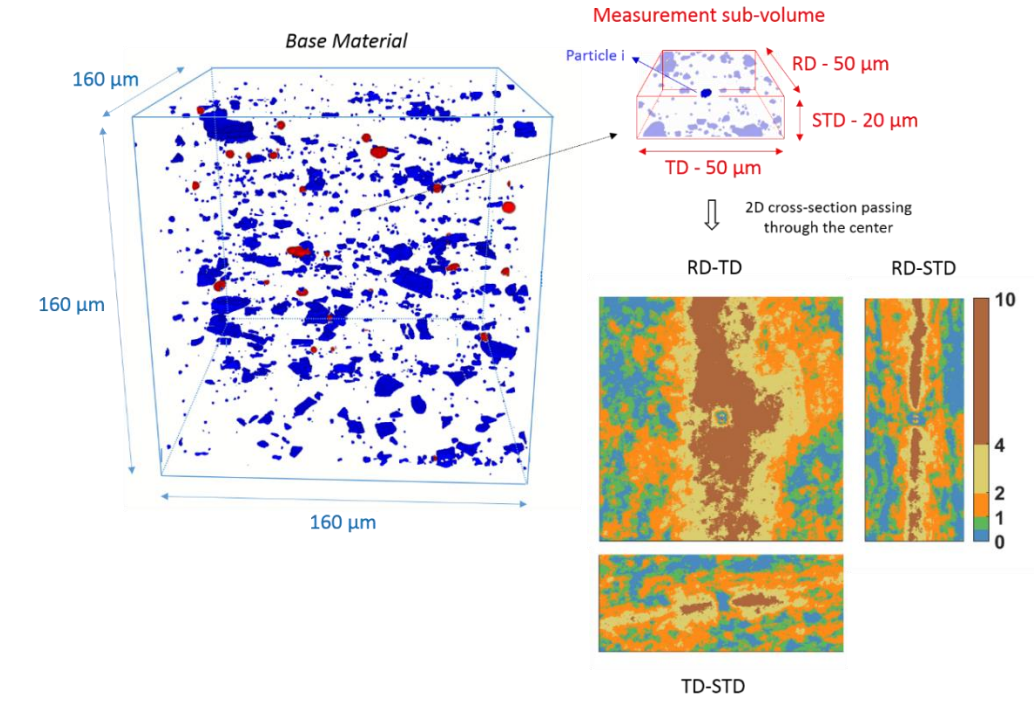

(a)

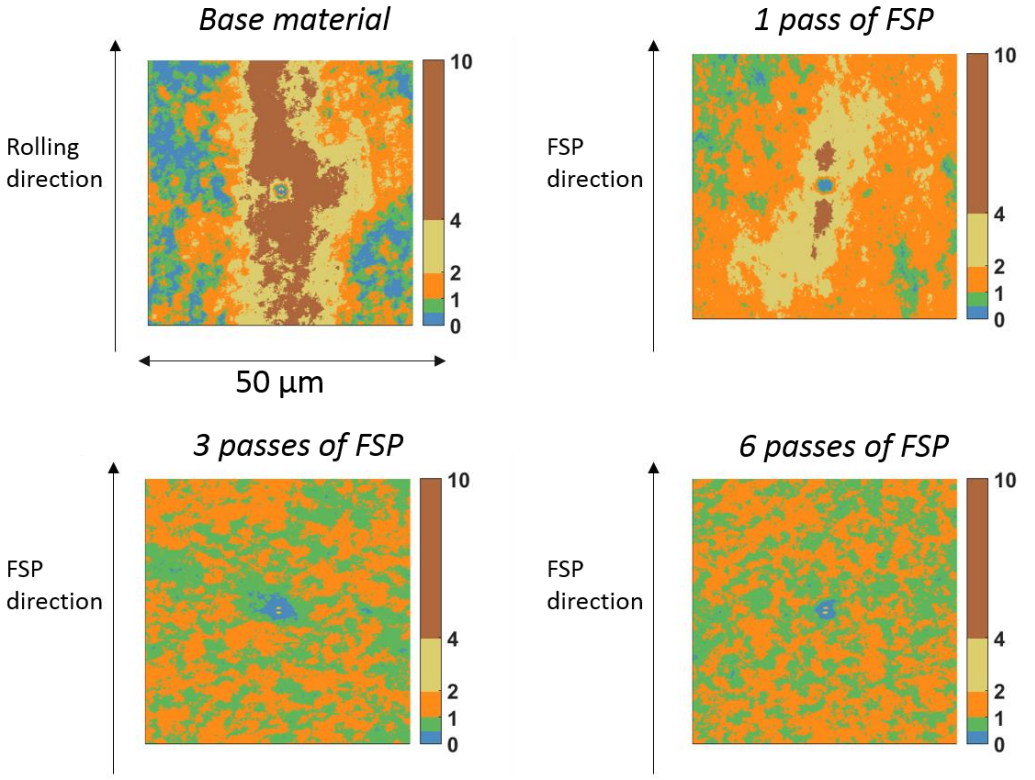

(b)

Figure 8 (a) Principle (left) and result (right) of the PCF analysis for the base material. On the left figure, intermetallic particles are presented in blue and voids in red. (b) Pair correlation functions (PCFs) from experimental images for the RD-TD plane through the center of the sub-volume for the base material and FSPed samples. PCF value smaller or larger than one corresponds respectively to a smaller or larger probability to find a neighbor in the vicinity of a particle compared to a perfectly homogenous distribution.

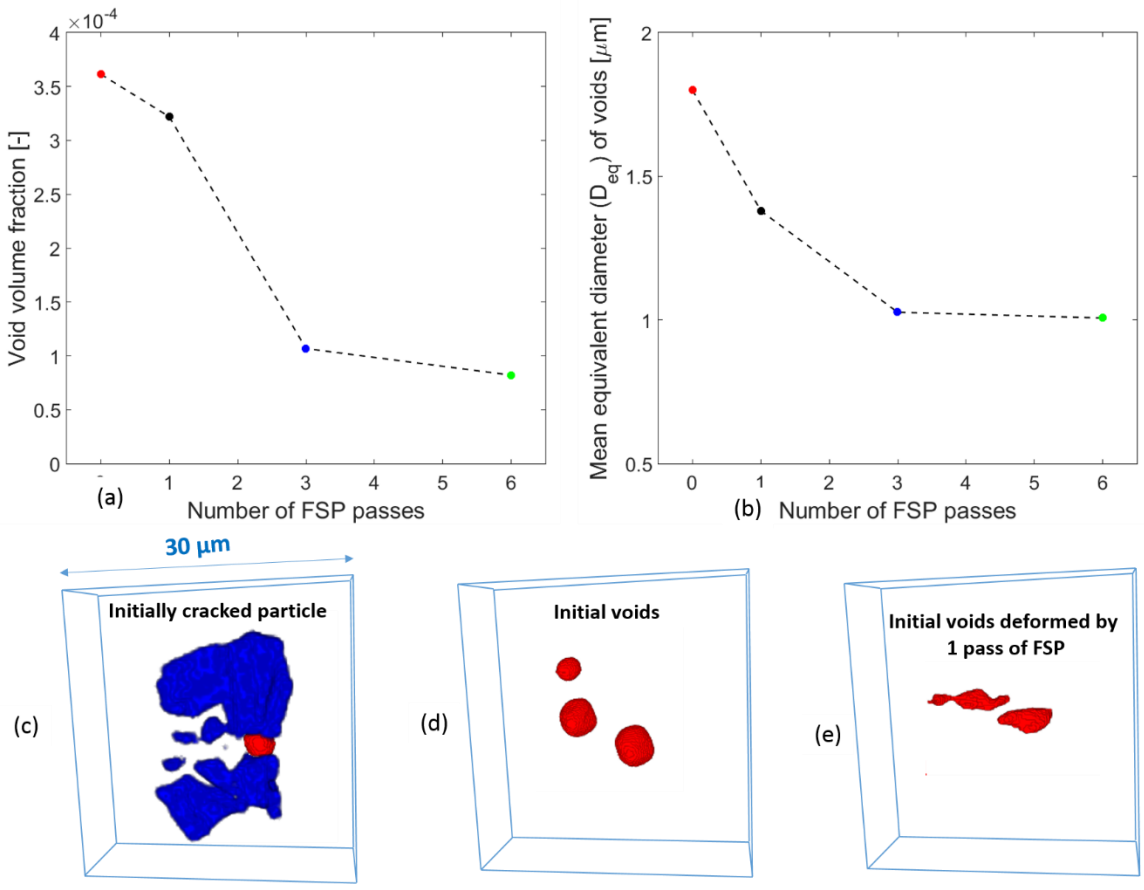

Figure 9. Evolution of (a) porosity volume fraction and (b) mean equivalent diameter of the voids as a function of the number of FSP passes. 3-D views of (c) an initially broken particle (blue) in the BM, (d) initial porosity in the BM and (e) voids observed after 1 pass of FSP. Cavities are in red.

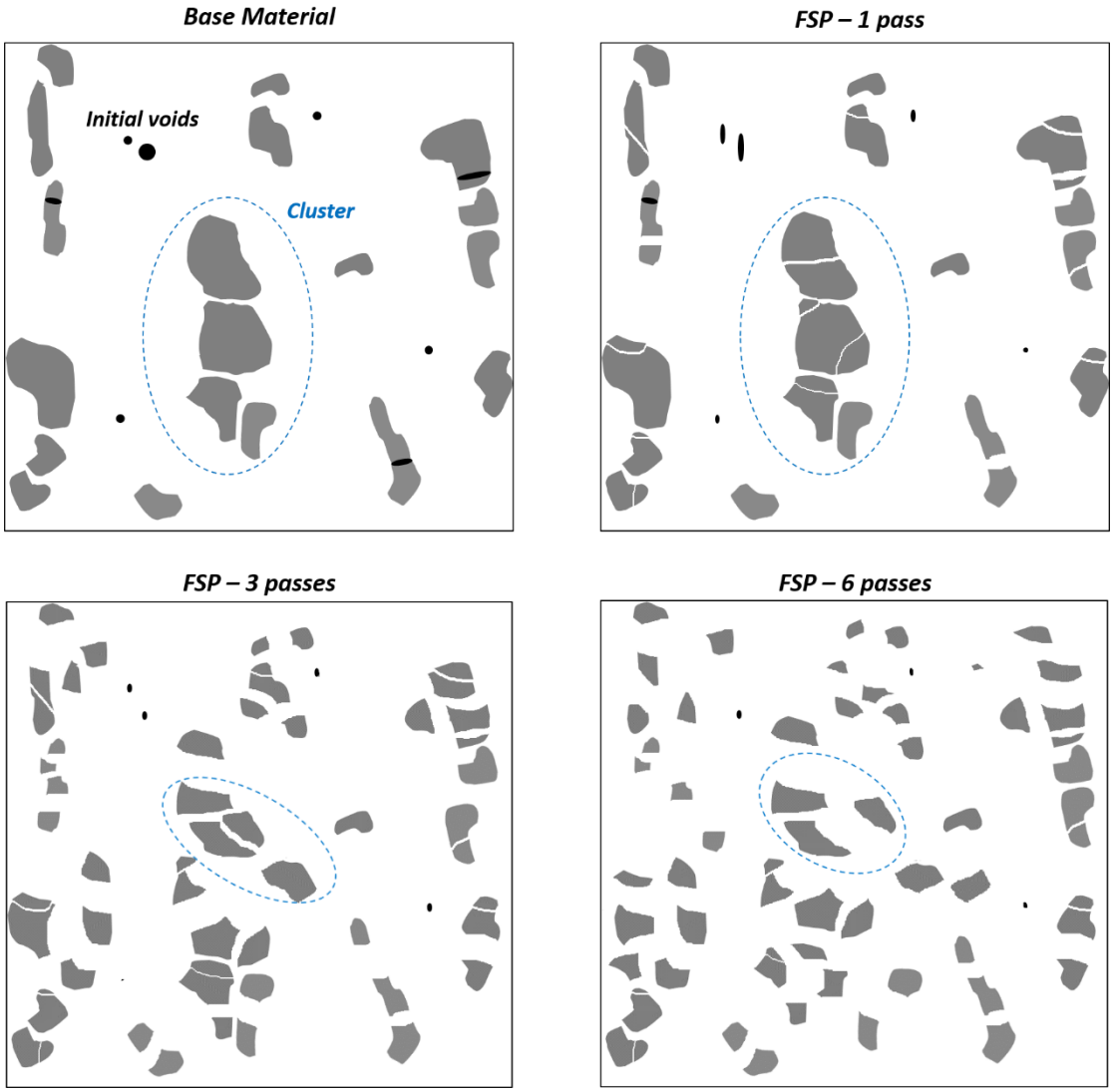

Figure 10. Schematic scenario of the microstructural evolution with the number of FSP passes.

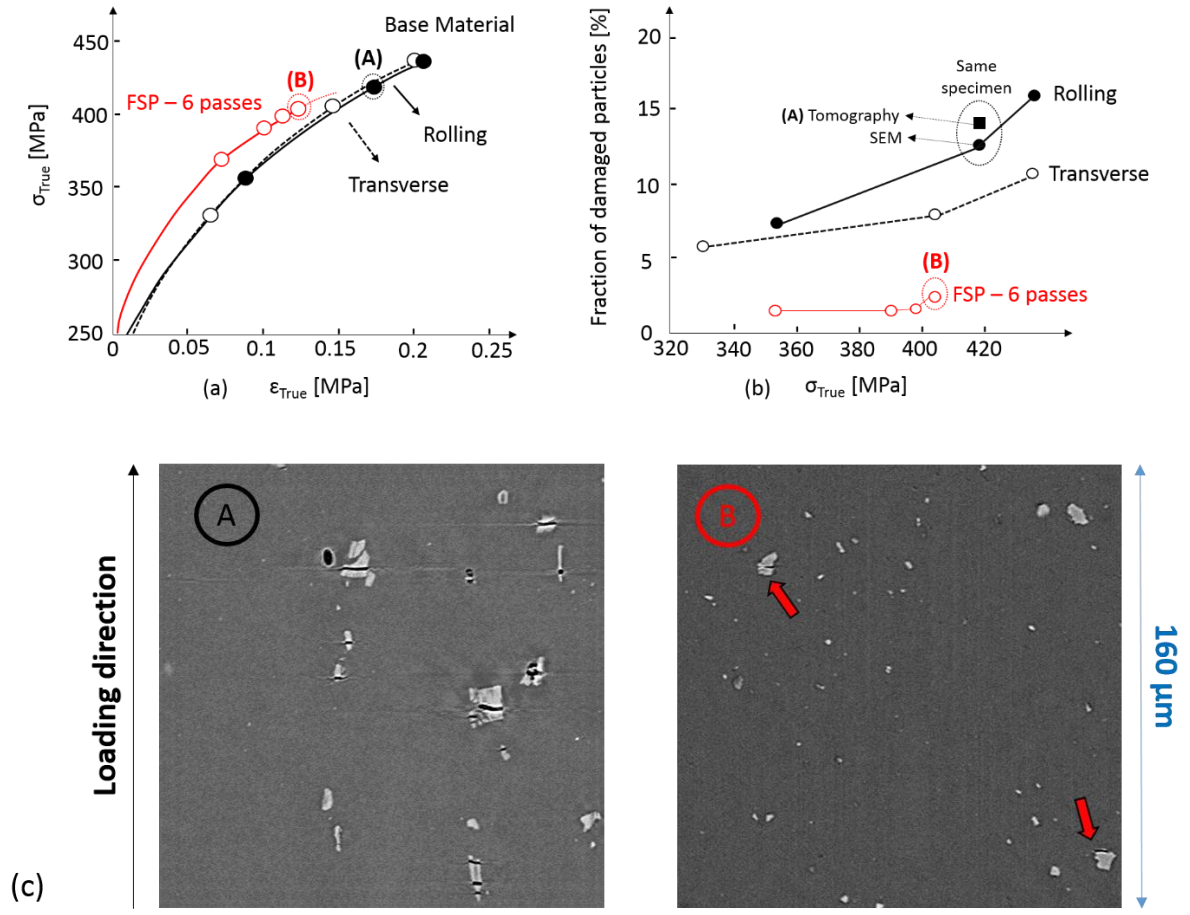

Figure 11. (a) Tensile curves of the base material loaded in the rolling and transverse direction, and after 6 FSP passes in the rolling direction. The base material is in the T4 state, and the FSPed material has been aged for 1 hour at 180°C. Each point corresponds to an interrupted tensile test and the fraction of damaged particles is given in (b). (c) X-ray microtomography reconstructed images of the two samples (A) and (B).

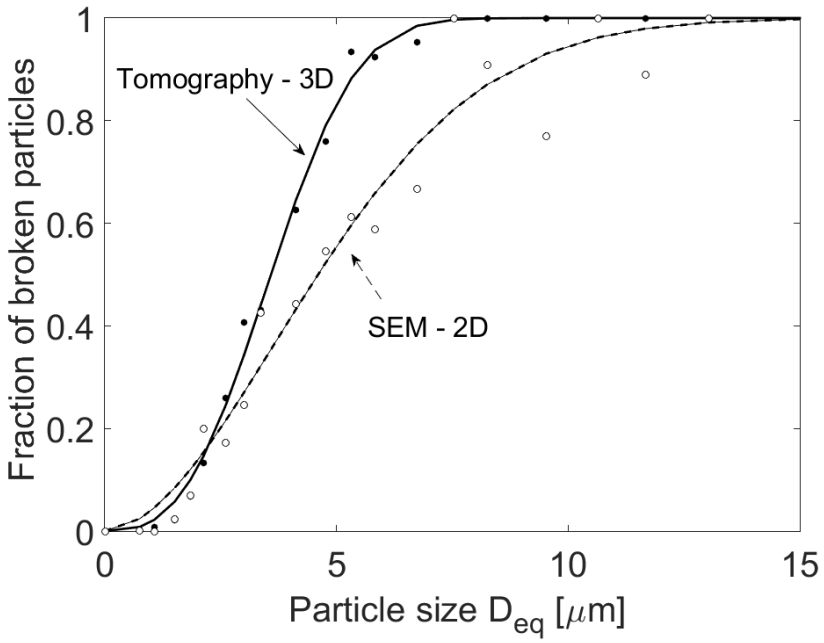

(a)

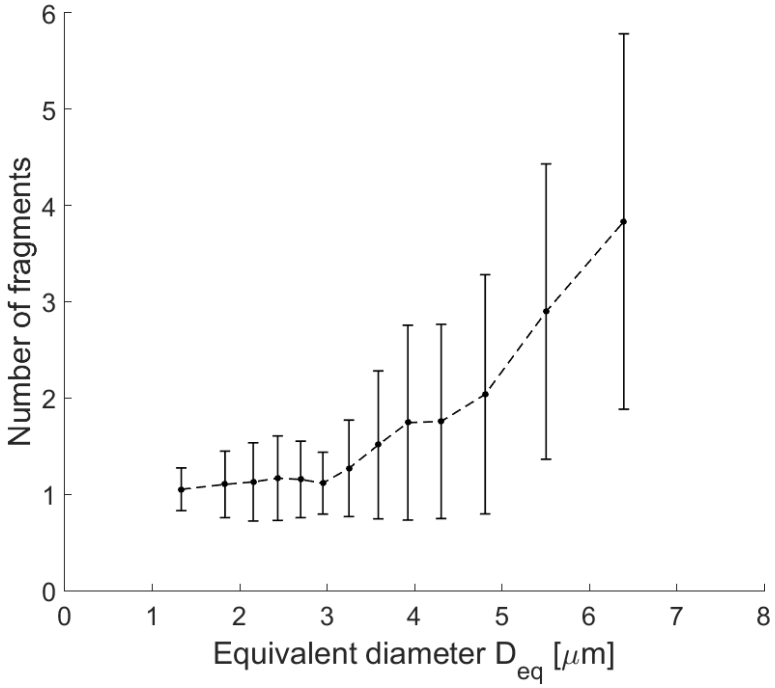

(b)

Figure **12**. Results obtained on the interrupted tensile test on BM, in the T4 state, loaded in RD up to 420 MPa and characterized by microtomography: (a) Fraction of broken particles as a function of the equivalent particle diameter (i.e. size) obtained from SEM analysis (over 2,000 particles analyzed) and microtomography (over 10,000 particles analyzed). (b) Number of observed fragments as a function of the size of the broken particles.

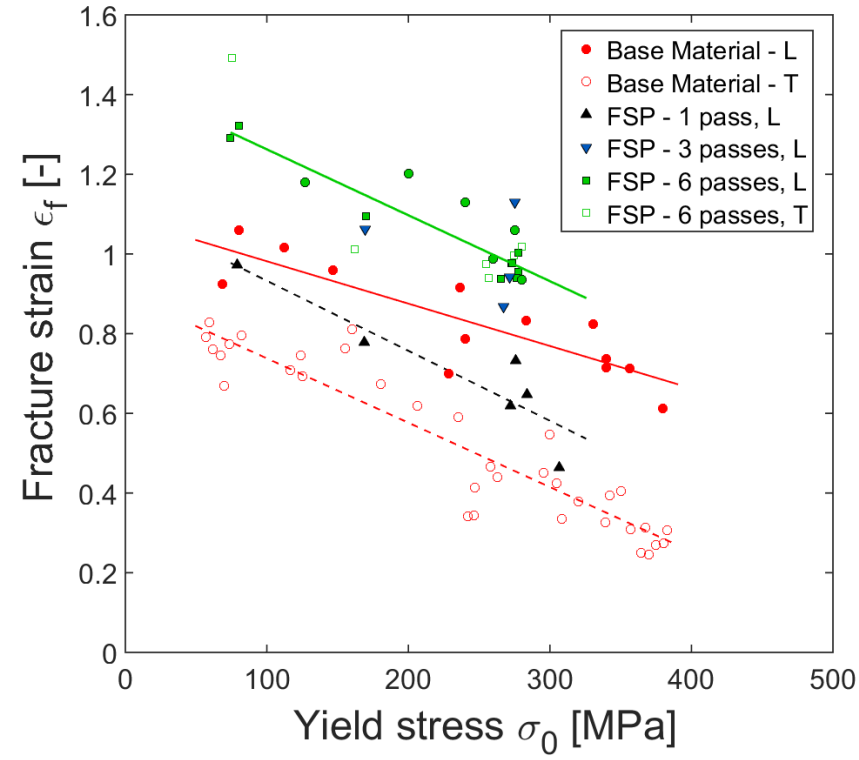

(a)

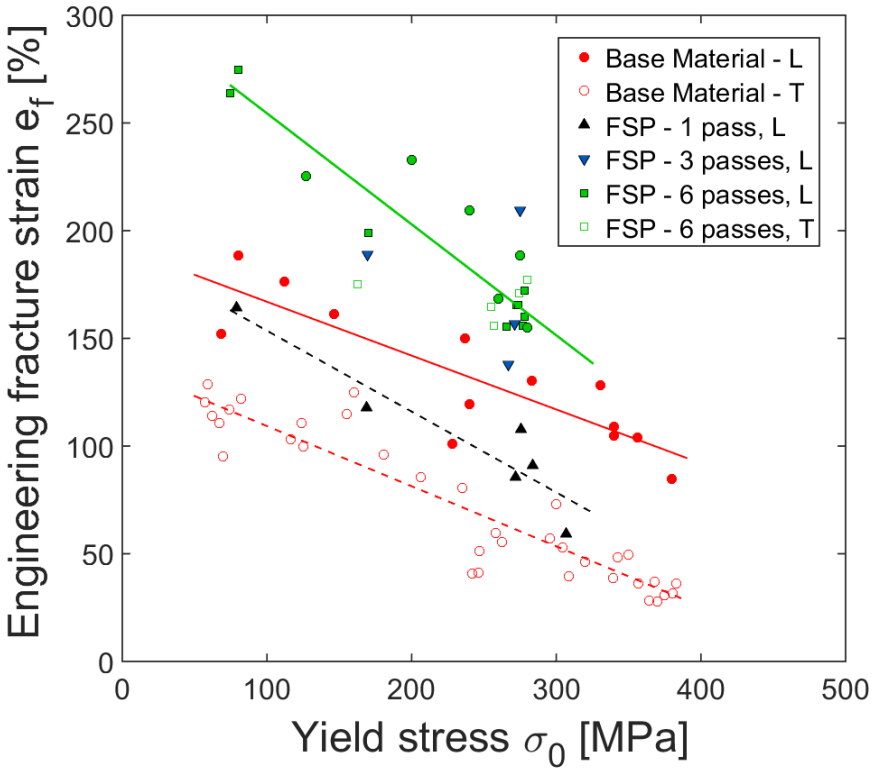

(b)

Figure 13. Variation of the (a) true fracture strains and (b) engineering fracture strain extracted from the uniaxial tensile tests as a function of the yield stress corresponding to the different heat treatments.

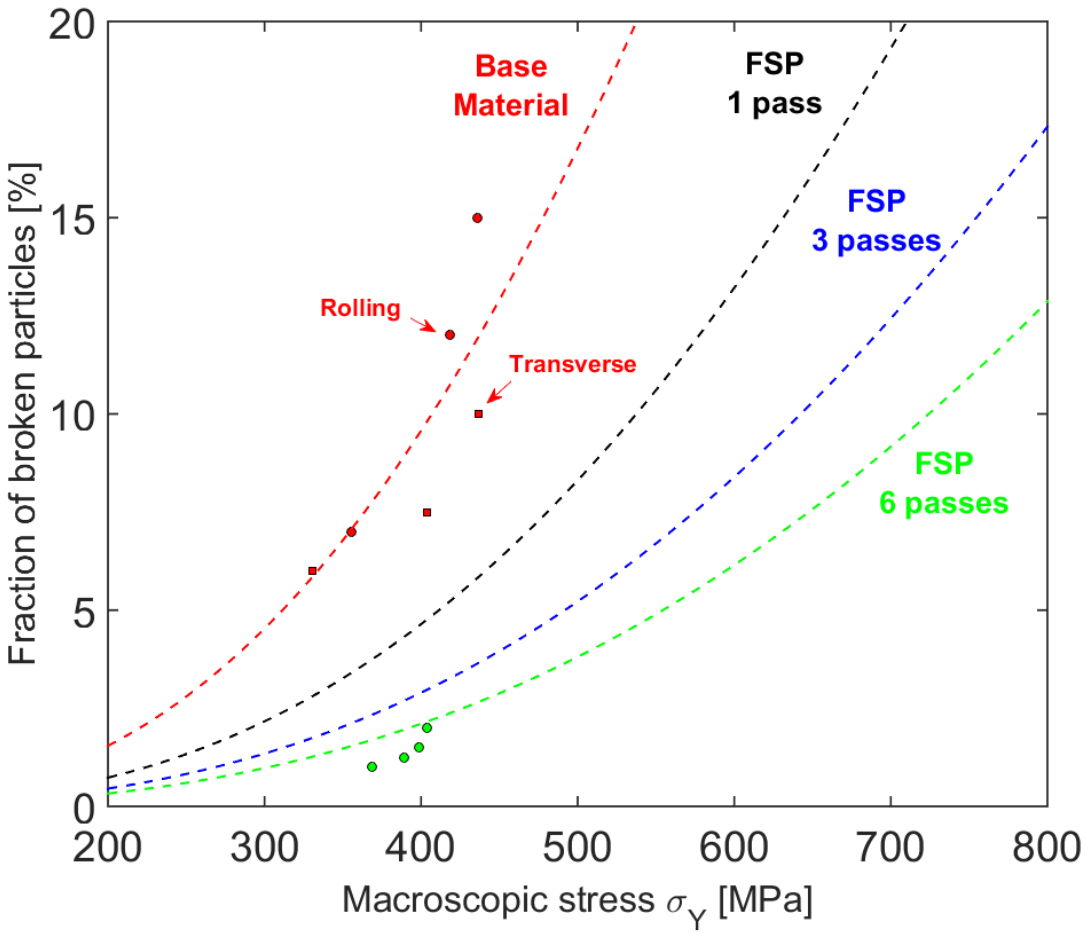

Figure 14. Fraction of broken particles as a function of the macroscopic flow stress. Comparison of experimental results (points) with the nucleation model (lines).

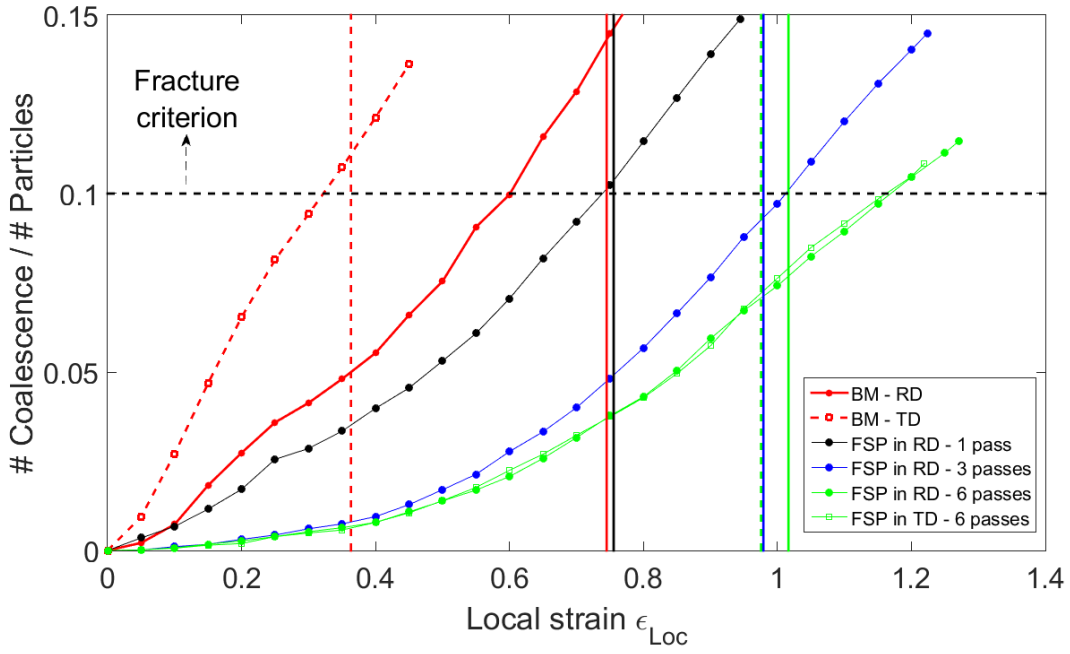

(a)

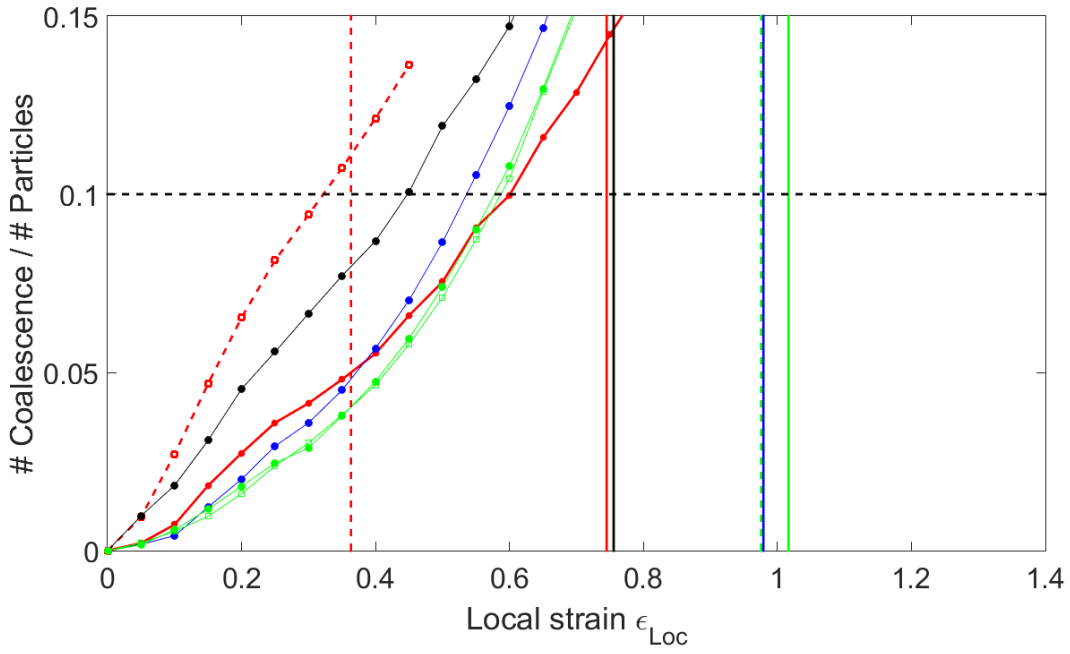

(b)

Figure 15. Results of the model applied on the T4 state. Ratio between the number of cavities couples satisfying the coalescence criterion and the number of particles, for the model (a) with and (b) without the effect of particle size on void nucleation. The vertical lines indicate the experimental fracture strain (ε_f).